

Exploring X-ray and radio emission of type 1 AGN up to $z \sim 2.3^\star$

L. Ballo¹, F.J.H. Heras^{1, **}, X. Barcons¹, and F.J. Carrera¹

Instituto de Física de Cantabria (CSIC-UC), Avda. Los Castros s/n (Edif. Juan Jordá), E-39005 Santander (Spain)

Received XXXXXXXXXX XX, XXXX; accepted XXXXXXXXXX XX, XXXX

ABSTRACT

Context. X-ray emission from Active Galactic Nuclei (AGN) is dominated by the accretion disk around a supermassive black hole. The radio luminosity, however, has not such a clear origin except in the most powerful sources where jets are evident. The origin (and even the very existence) of the local bi-modal distribution in radio-loudness is also a debated issue.

Aims. By analysing X-ray, optical and radio properties of a large sample of type 1 AGN and quasars (QSOs) up to $z > 2$, where the bulk of this population resides, we aim to explore the interplay between radio and X-ray emission in AGN, in order to further our knowledge on the origin of radio emission, and its relation to accretion.

Methods. We analyse a large (~ 800 sources) sample of type 1 AGN and QSOs selected from the 2XMMi XMM-Newton X-ray source catalogue, cross-correlated with the SDSS DR7 spectroscopic catalogue, covering a redshift range from $z \sim 0.3$ to $z \sim 2.3$. Supermassive black hole masses are estimated from the Mg II emission line, bolometric luminosities from the X-ray data, and radio emission or upper limits from the FIRST catalogue.

Results. Most of the sources accrete close to the Eddington limit and the distribution in radio-loudness does not appear to have a bi-modal behaviour. We confirm that radio-loud AGN are also X-ray loud, with an X-ray-to-optical ratio up to twice that of radio-quiet objects, even excluding the most extreme strongly jetted sources. By analysing complementary radio-selected control samples, we find evidence that these conclusions are not an effect of the X-ray selection, but are likely a property of the dominant QSO population.

Conclusions. Our findings are best interpreted in a context where radio emission in AGN, with the exception of a minority of beamed sources, arises from very close to the accretion disk and is therefore heavily linked to X-ray emission. We also speculate that the radio-loud/radio-quiet dichotomy might either be an evolutionary effect that developed well after the QSO peak epoch, or an effect of incompleteness in small samples.

Key words. galaxies: active – X-rays: galaxies – quasars: general – quasars: emission lines – radio continuum: galaxies

1. Introduction

Strong X-ray and radio emissions are properties that distinguish active galactic nuclei (AGN) from the whole population of galaxies. X-rays are the most direct manifestation of the accretion disk around a supermassive black hole (SMBH) at the centre of the galaxy hosting the AGN. Although radio emission is most apparent in a fraction of AGN, in particular in those classified as “radio-loud” (RL), which constitute 10 – 20% of the local AGN population, recent work shows that even radio-quiet (RQ) AGN exhibit a radio-emitting core, which might result from some sort of radio plasma arising in the vicinity of the SMBH. While optical emission in AGN is due to the superposition of thermal components coming from different distances from the nucleus, with a contribution of radiation reprocessed outside the AGN central engine, both X-rays and radio emission can be used to probe the immediate environment of the SMBH.

From the observational point of view, two quantities appear most relevant in exploring the possible link between radio emission and accretion: the UV-based radio-loudness, defined as $\mathcal{R} \equiv F_{5\text{GHz, rf}}/F_{2500\text{\AA, rf}}$ (monochromatic fluxes in the rest frame; Stocke et al. 1992), and the Eddington ratio $\lambda_{\text{Edd}} \equiv L_{\text{bol}}/L_{\text{Edd}}$,

where L_{bol} is the bolometric luminosity and $L_{\text{Edd}} \equiv 1.3 \times 10^{38} M_{\text{BH}}/M_{\odot} [\text{ergs s}^{-1}]$ is the limiting luminosity of Eddington (Eddington 1913; Rees 1984). Obtaining these quantities requires radio, UV and X-ray fluxes, plus reliable bolometric corrections and SMBH mass (M_{BH}) estimates. In contradiction to earlier works, Ho (2002) showed that \mathcal{R} is uncorrelated with M_{BH} , but strongly anticorrelated with λ_{Edd} . This was interpreted by Ho (2002) in the framework of changes of the accretion mode, from a radiatively efficient standard accretion at $\lambda_{\text{Edd}} > 0.01$ to a radiatively inefficient ADAF (Advection Dominated Accretion Flow, which is prone to radio-emission) at lower Eddington ratios.

The local low-luminosity AGN population appears to show a dichotomy in radio-loudness, where two distinct populations appear to peak at $\mathcal{R} \sim 10 - 100$ (RL) and $\mathcal{R} \sim 0.1 - 1$ (RQ; Kellermann et al. 1989). This bimodality is not so apparent (or plainly non-existing) in deeper radio (White et al. 2000) or X-ray selected surveys (Brinkmann et al. 2000), where AGN samples display a continuous distribution in radio-loudness. It is then unclear whether there is something fundamentally different between strongly and weakly emitting radio AGN, and this is directly linked to the origin of radio emission in these objects.

With mass accretion rate largely regulating the luminosity of the AGN, the only other relevant parameter to modulate radio-loudness and whether an AGN develops or not a powerful jet, is the SMBH spin (Blandford 1990; Wilson & Colbert 1995). In a simple scenario where jets are formed in rapidly spinning SMBH, evolution by galaxy and associated SMBH mergers

Send offprint requests to: L. Ballo, e-mail: ballo@ifca.unican.es

* Tables 3–5 are only available in electronic form at the CDS via anonymous ftp to cdsarc.u-strasbg.fr (130.79.128.5) or via <http://cdsweb.u-strasbg.fr/cgi-bin/qcat?J/A+A/>

** Present Address: Department of Zoology, University of Cambridge, Downing St, Cambridge, CB2 3EJ, UK

would naturally lead towards a SMBH population with low spin (Berti & Volonteri 2008). This would imply that smooth accretion (which tends to spin up SMBH) would be unimportant in the history of SMBH growth. However, the dependence of RL fraction on redshift and luminosity is still a strongly debated issue (e.g., Jiang et al. 2007, and references therein): the number of RL sources in the analyzed samples, not large enough to study their two-dimensional distribution in redshift and luminosity, and the wide range of selection criteria used to define the samples observed contribute to a large range of contradicting results.

Sikora et al. (2007) extend this view by showing that the anticorrelation between \mathcal{R} and λ_{Edd} comes in two parallel tracks, one for RL AGN residing in elliptical galaxies and one (lower) for RQ AGN residing in spiral galaxies. They propose a revised spin paradigm, where elliptical galaxies (and thence RL AGN) host highly spinning SMBH as a result of at least one major merger in the past, while spiral galaxies (and thence RQ AGN) underwent mostly chaotic accretion, i.e., accretion of small mass fragments with random angular momenta. But since highly accreting luminous QSOs residing in ellipticals are largely RQ, speculations that radio emission might be intermittent have been put forward. Most recent versions of the spin paradigm call for retrograde systems (where the SMBH and the accretion disk counter rotate) as the mechanism to extract the most powerful jets (Garofalo et al. 2010). RL AGN are mostly assumed to be retrograde, and RQ prograde. Natural evolution tends to make all SMBH-accretion disk systems prograde, which would explain the overwhelmingly large fraction of RQ AGN in the local Universe.

The release of large catalogues of fairly deep X-ray and radio sources, along with the optical photometry and spectroscopy provided by the Sloan Digital Sky Surveys (SDSS; see Abazajian et al. 2009, for the final public data release from SDSS-II), calls now for a study of the relation between accretion and radio properties in large samples of AGN. This is of particular interest to infer the physical origin of the radio emission. In this study we use the incremental Second XMM-Newton Serendipitous Source Catalogue (2XMMi; Watson et al. 2009), which we correlate with the SDSS Data Release 7 (DR7) to select a sample of X-ray detected type 1 AGN and QSOs. In this way, we use independent data to estimate the bolometric luminosity (from the X-ray data and suitable bolometric corrections) and the SMBH mass that we estimate from the SDSS spectra using the Mg II broad emission line. The latter effectively limits our sample to $z \leq 2.3$, which is however enough to encompass the peak of the QSO activity epoch at around $z \sim 2$. Note that we do not include type 2 AGN in this study, in part because the mass estimates based on other proxies (e.g., the [O III] line width) are more uncertain and would compromise the homogeneity of our study. Radio information is obtained from the FIRST-VLA catalogue (Becker et al. 1995).

The paper is organized as follows. In Section 2 we describe the selection method used to generate the samples; Section 3 is devoted to recover the nuclear properties (i.e., SMBH masses, nuclear bolometric luminosities, and Eddington ratios). In Section 4 radio-loudness properties are discussed and compared with results from the literature. Finally, in Section 5 we summarize our work. Throughout this paper, a concordance cosmology with $H_0 = 71 \text{ km s}^{-1} \text{ Mpc}^{-1}$, $\Omega_\Lambda = 0.73$, and $\Omega_m = 0.27$ (Spergel et al. 2003, 2007) is adopted. The energy spectral index, α , is defined such that $F_\nu \propto \nu^{-\alpha}$. The photon index, defined as $N_\epsilon \propto \epsilon^{-\Gamma}$, where ϵ is the photon energy, is $\Gamma = \alpha + 1$.

2. Sample selection

The starting point for the present work is the cross-correlation of the 2XMMi with the SDSS DR7 carried out by Pineau et al. (2011).

The 2XMMi catalogue is an extended version of the 2XMM catalogue, covering $\sim 1\%$ of the sky (Watson et al. 2009); in their analysis, Pineau et al. (2011) considered only point-like sources having a positional error smaller or equal to $5''$, obtaining an initial sample of ~ 200000 unique 2XMMi sources.

To construct the initial list of optical candidate counterparts, among the more than 350 million distinct objects contained in the SDSS DR7 Photometric Catalog (Abazajian et al. 2009), only the so-called primary sources were considered. To perform the correlation, a query centred in the centre of the FOV of each XMM-Newton observation was then run, with a search radius equal to the distance from the centre to the farthest X-ray source increased by $3'$.

The counterpart identification was performed by computing a likelihood ratio, defined as the probability of finding the optical counterpart at a normalized distance r divided by the probability of having a spurious object at the same distance. The applied formalism, aimed at providing probabilities of identification based on positional coincidences only (no other information such as spectral energy distribution were used) led to 30055 X-ray sources with more than 90% probability of identification in the DR7. At this threshold, Pineau et al. (2011) estimated only 2% spurious matches and a 77% completeness.

We were interested in weighting the black hole in the centre of a sample of AGN using the width of optical lines emitted from the Broad Line Region (BLR), namely the Mg II $\lambda 2799 \text{ \AA}$ (see Sect. 3). Among the X-ray selected sources detected in the SDSS, we then considered objects that were targets of optical spectroscopic follow-up in the SDSS, and classified as QSO or GALAXY¹ (specClass parameter equal 3 or 2, respectively²). Among those, we limited ourselves to the 906 showing in their spectra a Mg II line broad enough to have its origin in the BLR, specifically $\text{FWHM}(\text{Mg II}) > 900 \text{ km s}^{-1}$.

Recently, Shen et al. (2011) presented a compilation of properties of the sources in the SDSS DR7 quasar catalogue (Schneider et al. 2010); 892 out of the 906 sources just mentioned are in this catalogue, the rest being Seyfert galaxies. The fit to the Mg II line in 28 of those 892 provides null values for the FWHM or the M_{BH} : we then removed these sources from our sample. We are therefore left with 878 X-ray selected type 1 AGN (864 QSOs and 14 with Seyfert-like luminosity).

We collected information about radio emission for our sample by cross-correlating it with the Faint Images of the Radio Sky at Twenty-cm (FIRST; Becker et al. 1995) survey. The sky coverage of the FIRST survey implies that only 837 sources (823 QSOs) out of 878 fall in the FIRST fields, with 100 detections (98 among the QSOs). Being interested in studying the radiation arising from their nuclear regions, only the core emission should be considered. Following Shen et al. (2011), 27 out of 98 radio-detected QSOs have multiple FIRST source matches within $30''$. Comparing the contribution to the radio emission at the SDSS source position expected from the different FIRST components, we found that for all but one of these QSOs with multiple matched FIRST sources, the off-nuclear contamination is not negligible ($\gtrsim 1\%$): these 26 not core-dominated QSOs

¹ We do not consider HIZ-QSO (specClass = 4), whose high redshift ($z > 2.3$) implies the exit of the Mg II line from the SDSS spectrum.

² See <http://cas.sdss.org/astrodr7/en/help/docs/enum.asp?n=SpecClass>

Table 1 Summary of the samples.

	“main sample”	“control sample”
TOTAL	852	4508
in FIRST	811	4508
(radio det. - radio undet.)	(74 - 737)	(4508 - 0)
Radio class.: RL	59	3796
non-RL	15	702
det. RI	443	0
$1 < R^{up,lim} \leq 10$	7	10
RQ	287	0
n.c.		
in ROSAT	69	501
in ROSAT & in FIRST	67	501
(radio det. - radio undet.)	(13 - 54)	(501 - 0)
Radio class.: RL	9	398
non-RL	4	99
det. RI	35	0
$1 < R^{up,lim} \leq 10$	5	4
RQ	14	0
n.c.		

were therefore removed. A visual inspection of the FIRST images confirms that the rest of the detected QSOs and the 2 radio-detected sources with Seyfert-like luminosity have only one FIRST source within the FIRST resolution.

Our final sample (hereafter, “main sample”) is composed by 852 X-ray selected type 1 AGN (838 QSOs and 14 with Seyfert-like luminosity); out of them, 811 fall in the FIRST fields, with 74 detections (72 among the QSOs). A summary of this sample is presented in Table 1.

Basic information is listed in Table 3, only available in electronic form at the CDS³; for convenience of the reader, we show here a portion. As noted before, the requirement of covering with the SDSS spectra an energy range containing the Mg II line imply a cut in distance; our sources have redshifts more or less uniformly distributed between 0.3 and 2.3 (see Fig. 1, left panel). In Figure 1 (right panel) the sample distribution in the optical–X-ray flux plane is reported.

We note that the main characteristic of our sample is to be X-ray-selected. In order to check for possible selection biases, and to test our findings in terms of nuclear properties, we constructed a “control sample” by searching for SDSS radio sources matching the same optical constraints adopted to construct our main sample, either falling in a region not covered by XMM-Newton, or not detected in X-rays. We found 5888 objects in the SDSS-FIRST cross-correlation having Mg II line widths and optical spectroscopic classifications satisfying the criteria previously described, not included in the 2XMMi catalogue; 5548 of them are classified as QSOs by Schneider et al. (2010). Rejecting the 188 QSOs for which Shen et al. (2011) do not provide valid black hole masses from the Mg II line, we are left with 5700 sources. In the same way as we have done for the “main sample”, we calculated the off-nuclear contamination for the 1196 sources showing multiple matches in the FIRST images within 30”; this analysis drove us to remove from the sample all but four not core-dominated AGN. The “control sample” is therefore composed by 4508 radio-detected type 1 AGN (4204 QSOs and 304 with Seyfert-like luminosity); their redshift distribution is overplotted in Figure 1 (left panel), while their classification in terms of radio properties is summarized in Table 1.

Only 11 out of this “control sample” (7 classified as QSOs) fall in one or more of the XMM-Newton fields used to construct the 2XMMi, and show positive “good exposure time” in at least

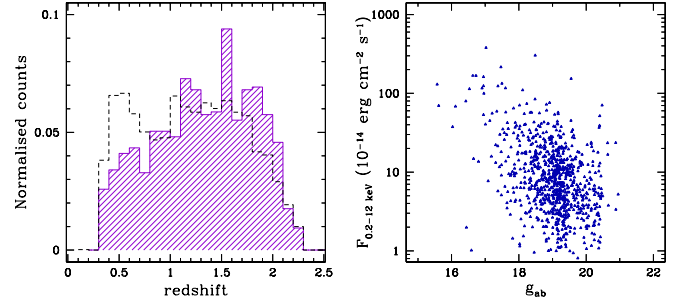


Fig. 1 Properties of the X-ray selected type 1 AGN in our sample. *Left panel*: Normalized distribution in redshift (magenta shaded histogram); the black dashed line shows the distribution for the “control sample”. *Right panel*: Total X-ray fluxes vs. g-band AB magnitudes.

one of the EPIC cameras. Thanks to FLIX⁴, the flux upper limit server for XMM-Newton data provided by the XMM-Newton Survey Science Center (SSC), we obtained for all these X-ray undetected AGN an upper limit in the 0.2 – 12 keV flux. Basic information for these 11 sources is reported in the second part of Table 3.

From this point of view, useful information can be obtained considering the match between the two samples and the ROSAT All-Sky Survey (RASS; Voges et al. 1999). In the “main sample”, 13 out of the 69 ROSAT-detected sources are radio-detected; 501 objects in the “control sample” are ROSAT-detected.

3. Recovering the nuclear properties

The spectral information provided by the 2XMMi and the SDSS DR7 catalogues has been used to study the nuclear activity of the galaxies in our sample. The black hole (BH) masses were derived from the optical measurements (continuum and line width), while we estimated the bolometric luminosity from the X-ray flux. The use of data from different energy ranges allows an independent determination of the two parameters. A discussion of the error estimates is presented in Sect. 3.4. Optical- and radio-based parameters have been calculated also for the “control sample”; X-ray-based quantities have been obtained for the 11 sources for which upper limits to the X-ray flux were obtained.

3.1. Black hole masses

For each source, the mass of the central compact object was estimated from the so-called mass-scaling relations using broad-emission-line widths and nuclear continuum luminosities (Kaspi et al. 2000, 2005; Vestergaard & Peterson 2006; Vestergaard et al. 2008, and references therein). Being interested in exploring in a uniform way (i.e., using the same proxy for all the sources) the BH masses and accretion rates in a sample of AGN extended up to (relatively) high redshift, the best choice is the relation based on the Mg II emission line. For the subsample of QSOs, we adopted the mass obtained by Shen et al. (2011,

³ See <http://cdsweb.u-strasbg.fr/A+A.htx>

⁴ See <http://www.ledas.ac.uk/flix/flix.html>

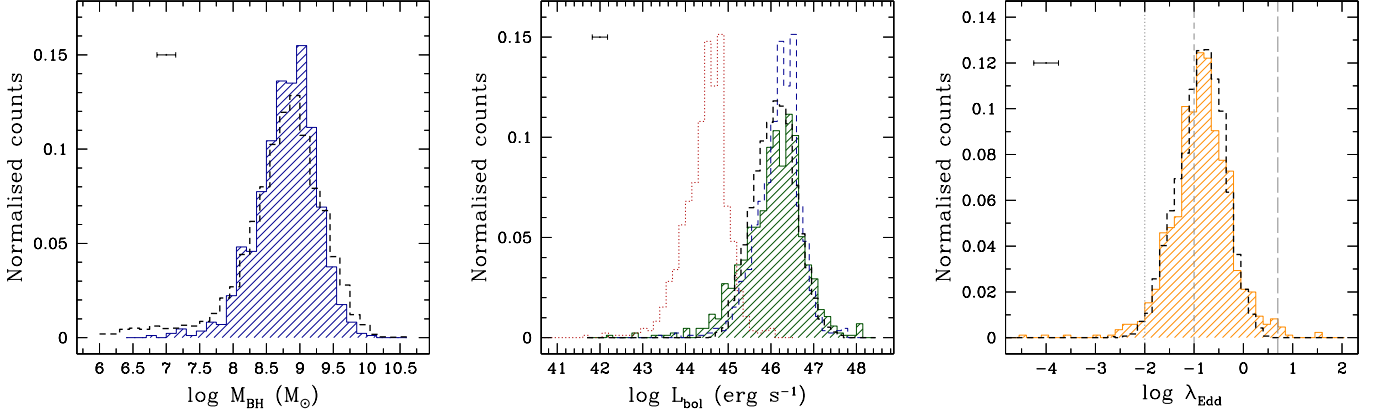


Fig. 2 Nuclear properties, derived as described in Sect. 3; the error bars reported represent the mean uncertainties obtained as detailed in Sect. 3.4. *Left panel*: Normalized distribution in BH mass (blue shaded histogram); the black dashed line shows the distribution for the “control sample”. *Central panel*: Distribution in bolometric luminosity obtained assuming the luminosity-dependent $\kappa_{2-10\text{ keV}}$ in equation (2), green shaded histogram; the red dotted line and the blue dashed line represent the distributions in bolometric luminosity obtained assumed a constant $\kappa_{2-10\text{ keV}} = 1$ (i.e., the distribution of the intrinsic hard X-ray luminosity) and $\kappa_{2-10\text{ keV}} = 50$, respectively. The black dashed line shows the distribution in bolometric luminosity for the “control sample”, computed from optical/UV luminosities (Shen et al. 2011). *Right panel*: Distribution in Eddington ratio (yellow shaded histogram); the black dashed line shows the distribution in Eddington ratio for the “control sample” (Shen et al. 2011). Grey dotted, dashed, and long-dashed vertical lines define the regions of $\lambda_{\text{Edd}} < 0.01$, $0.1 < \lambda_{\text{Edd}} < 5$, and high-super-Eddington accretion, respectively.

LOGBH_MGII_V009 column in their catalogue) adopting the re-calibration proposed by Vestergaard & Osmer (2009):

$$M_{\text{BH}} = 10^{6.86} \left[\frac{\text{FWHM}(\text{Mg II})}{1000 \text{ km s}^{-1}} \right]^2 \left[\frac{\lambda L_{\lambda}}{10^{44} \text{ ergs s}^{-1}} \right]^{0.5} \quad (1)$$

for $\lambda = 3000 \text{ \AA}$, with a 1σ scatter in the logarithmic zero-point of 0.55 dex.

For the 14 X-ray selected AGN (and for the 304 sources in the “control sample”) not present in the QSO catalogue, we adopted the same relation; the intrinsic FWHM was obtained from the observed standard deviation of the Mg II line, as reported in the SDSS catalogue, while the monochromatic continuum luminosity was estimated using a typical QSO template. We adopted the composite spectrum provided by P. Francis⁵ in 2002, updating the original template presented by Francis et al. (1991). To normalize the template, we used the continuum flux observed under the line, as reported in the SDSS catalogue (see Table 3). The derived line widths, continuum luminosities, and BH masses are reported in Table 4 (also in this case, the entire table is available in electronic form). We found rather high masses, narrowly distributed between $\sim 10^8$ and $\sim 3 \times 10^9 M_{\odot}$ (see Fig. 2, *left panel*; the distribution for the “control sample” is overplotted).

3.2. Bolometric luminosities

Concerning the bolometric luminosity, several bolometric corrections, starting from the emission at various wavelengths, can be found in the literature. The results obtained from such relations must be taken with care, being based on average SEDs, assumed to describe the broad-band emission of quite different sources; moreover, the emission observed in each energy range could be affected by contamination due to different external and/or reprocessed components, and these contributions

could be extremely difficult to evaluate. Nevertheless, they provide a powerful tool to investigate the physics of the nucleus. Here, we took advantage of having high-energy information, directly linked to the AGN innermost regions and less affected by obscuration. We derived the hard X-ray luminosity in the 2 – 10 keV energy range from the EPIC-pn 0.2 – 12 keV flux (provided in the 2XMMi catalogue) corrected for the Galactic absorption, assuming as intrinsic emission a power law with Γ fixed to 1.9.

Note that in case of absorption, the intrinsic emission would be more intense than estimated here; a similar result would be produced if the real observed spectrum is flatter than 1.9. Therefore, the X-ray luminosity adopted here can be in principle lower than the intrinsic one (see e.g. Panessa et al. 2006). From the analysis of the hardness-ratios presented in Sect. 4.1, we expect a mean correction factor $L_{2-10\text{ keV}}^{\text{abs,PL}}/L_{2-10\text{ keV}}^{\text{PL}}$ of ~ 1.1 , with a maximum value of ~ 2.8 .

To estimate the bolometric luminosity, we assumed the luminosity-dependent X-ray bolometric correction ($\kappa_{2-10\text{ keV}} \equiv L_{\text{bol}}/L_{2-10\text{ keV}}$) following Marconi et al. (2004):

$$\log(L_{\text{bol}}/L_{2-10\text{ keV}}) = 1.54 + 0.24(\log L_{\text{bol}} - 45.58) + 0.012(\log L_{\text{bol}} - 45.58)^2 - 0.0015(\log L_{\text{bol}} - 45.58)^3 \quad (2)$$

with a 1σ scatter ~ 0.1 (taken by the authors to be independent of the luminosity).

In Figure 2 (*central panel*) we present the distribution of bolometric luminosities (green shaded histogram; the red dotted line superimposed represents the distribution of intrinsic X-ray luminosity in the 2 – 10 keV energy range. The former is clearly broader, as expected due to the assumption of an increasing luminosity-dependent bolometric correction. The effects of possible intrinsic absorption on the bolometric luminosities are slightly higher than in the case of the X-ray luminosity, although still rather low (mean correction factor $L_{\text{bol}}^{\text{abs,PL}}/L_{\text{bol}}^{\text{PL}} \sim 1.2$, with a maximum value of ~ 4.2).

⁵ See <http://msowwww.anu.edu.au/pfrancis/composite/widecomp.d>

Our results critically depend on the bolometric luminosities recovered, then in turn on the correction applied to the X-ray luminosities. The selection of the best X-ray bolometric correction is not a trivial issue. Depending on the studied sample, the range of the electromagnetic spectrum used to reconstruct the SEDs, and whether the reprocessed emission was considered, different solutions have been proposed. Some authors considered luminosity-dependent $\kappa_{2-10\text{keV}}$, (e.g., Marconi et al. 2004; Hopkins et al. 2007), suggesting changes in the physics of the disk-corona system with the intensity of the nuclear emission, whereas others found corrections with a very shallow or absent correlation with X-ray luminosity (e.g., Elvis et al. 1994; Richards et al. 2006; Marchese et al. 2012). As expected due to the luminosity-dependent expression adopted, the $\kappa_{2-10\text{keV}}$ distribution shows a significant spread (ranging from ~ 5 up to few hundred). However, although slightly broadened at low values, our distribution of L_{bol} from the luminosity-dependent correction from Marconi et al. (2004) is roughly consistent with that obtained assuming a mean constant value $\kappa_{2-10\text{keV}} = 50$ (see Fig. 2, *central panel*, blue dashed line).

Although their origin in the innermost region of the AGN makes the X-rays the most direct proxy of the total emission, we have reworked our calculations with the bolometric luminosities obtained from optical/UV observations. We considered the values reported by Shen et al. (2011), computed from optical/UV continuum luminosities at different wavelength depending on the source redshift, $L_{5100\text{\AA}}$ at $z < 0.7$, $L_{3000\text{\AA}}$ at $0.7 \leq z < 1.9$, and $L_{1350\text{\AA}}$ at $z \geq 1.9$, and adopting the bolometric corrections from the composite SED in Richards et al. (2006). As noted by the authors, the global SED from Richards et al. (2006) also counts the infrared (IR) bump in estimating the bolometric corrections; removing the IR radiation, assumed to come from the reprocessed UV radiation, reduces the bolometric corrections by about one third. In the same way, we estimated a bolometric luminosity for the QSOs in the “control sample”, which lack X-ray information; its distribution is overplotted as black dashed line in Figure 2 (*central panel*). In Figure 3, for the QSOs in the “main sample” we compare our X-ray based L_{bol} with that derived from the optical/UV, with the correction for the IR contribution applied. We note a slight departure from the one-to-one relation for sources with important radio emission with respect to the optical/UV radiation (RL; see below) in the highest redshift bin ($z \geq 1.9$). Nevertheless, the good agreement found for these objects among the two estimates of L_{bol} (consistent at a 3σ level) over a significant range in luminosity reassures us on the reliability of our approach.

3.3. Eddington ratios

The analysis performed allowed us to investigate the accretion powering these systems. In particular, Eddington ratios λ_{Edd} can be calculated as the ratio between bolometric and Eddington luminosities, where $L_{\text{Edd}} \equiv 1.3 \times 10^{38} M_{\text{BH}}/M_{\odot} [\text{ergs s}^{-1}]$ represents the exact balance between inward gravitational force and outward radiation force acting on the gas. Since the AGN luminosity is directly proportional to the accretion rate, λ_{Edd} is a measure of the accretion rate relative to the critical Eddington value.

We found rather high Eddington ratios (see Fig. 2, *right panel*, and last column in Table 4): for more than half of the “main sample” we found λ_{Edd} between 0.1 and 1, while only 3% show $\lambda_{\text{Edd}} \leq 0.01$. If we were to correct X-ray luminosities for the intrinsic absorption estimated from the hardness-ratio analy-

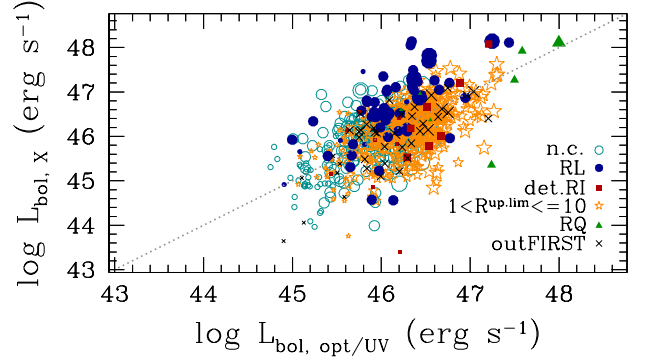


Fig. 3 L_{bol} inferred from X-ray luminosity vs. L_{bol} derived from the optical/UV continuum for the sub-sample of QSOs (Shen et al. 2011). Different symbols mark radio classification (see Sect. 4): not classified, light-blue open circles; RL, blue filled circles; detected RI, red filled squares; undetected sources with $R^{\text{up},\text{lim}} \in (1, 10]$, yellow open stars; RQ, green filled triangles; out of FIRST, black crosses. The symbol size increases with the redshift ($z < 0.7$, $0.7 \leq z < 1.9$, and $z \geq 1.9$), therefore identifying the continuum wavelength adopted to obtain the bolometric luminosity (see the text). The dotted line marks the one-to-one relation between the luminosities.

sis, would only increase λ_{Edd} . No significant trend with the redshift is observed (see Fig. 4).

Super-Eddington accretion is found for 54 sources. Luminosities exceeding the Eddington limit can be observed if accretion is not spherically symmetric (Osterbrock 1989); it has been suggested that accretion disks with radiation-driven inhomogeneities could produce luminosities exceeding the Eddington value (Begelman 2002). Eddington ratios close to, or even higher than, unity are often estimated for the subclass of Narrow-line Seyfert 1 galaxies (e.g., Collin et al. 2002; Collin & Kawaguchi 2004).

3.4. Error budget

Among the measurements obtained from the different catalogues used in this work, error estimates are available for the FWHM(Mg II), the X-ray flux in the 0.2 – 12 keV energy range observed frame, and the radio flux at 1.5 GHz observed frame. Moreover, in our determination of the nuclear parameters, we made a number of assumptions that must be taken into account when discussing the global uncertainties.

Errors for the M_{BH} are provided by Shen et al. (2011, LOGBH_MGII_V009_ERR column in their catalogue); for the sources not comprised in their catalogue (in the “main sample” and in the “control sample”, 14 and 304 objects, respectively), the errors are evaluated considering three different contributions⁶:

- The uncertainties associated with the width of the Mg II line, provided by the SDSS catalogue, typically of the order of $\leq 40\%$.
- A systematic error induced by the selection of one spectral shape common to all the sources for the optical emission: for each source, starting from a spectral shape $F_{\lambda} \propto \lambda^{\beta}$ we determine the scatter in the optical luminosity due to a different

⁶ We note that no errors on the flux under the line are provided in the SDSS tables.

choice in the slope ($\beta = -1.37 \pm 0.25$, averaging out the rest-frame spectra of 215 *SDSS* QSO; F. Fontanot, priv. comm.). The scatter in the L_λ (@3000 Å), calculated assuming as a pivot the flux below the Mg II line, is of $\sim 1.7\%$.

- The scatter in the phenomenological relation described by equation (1).

When propagated to yield the uncertainties of the BH masses, the third factor always prevails over the first two. Considering the whole “main sample”, the uncertainties on M_{BH} are lower than 37%

Uncertainties in the optical fluxes at 2500 Å and 4400 Å rest-frame (see Sect. 4) were obtained assuming again $\Delta\beta = \pm 0.25$ for the slope in the optical continuum, with fluxes below the Mg II and H β 4861 Å lines as pivot, respectively. The resulting scatters are $\sim 2.8\%$ and $\sim 2.5\%$, respectively.

We identify two possible sources of uncertainty in our estimate of the bolometric luminosity:

- The error in the normalization in equation (2).
- The uncertainties in the X-ray luminosities, obtained from the error on the flux provided by the 2XMMi catalogue. This contribution affects the bolometric luminosities in a non-linear way, given the luminosity-dependent bolometric correction.

The resulting uncertainties on $\log L_{\text{bol}}$ are lower than 5%; through quadratical sum propagation, we obtain a mean error on $\log \lambda_{\text{Edd}}$ of ~ 0.5 .

Finally, for the radio flux we need to combine two sources of error:

- The uncertainties associated with the FIRST radio flux.
- A systematic error induced by the selection of one spectral index common to all the sources (see Sect. 4), estimated assuming a change in the radio spectral index of $\sim 25\%$.

The relative errors, $\sigma_{F_{5\text{GHz}}}/F_{5\text{GHz}}$, are lower than 28% for both the 74 radio-detected sources and the 737 radio-undetected sources, for which we assumed the flux limit of the FIRST survey (see Sect. 4), respectively. This translates in the following mean relative errors for the radio-loudness and the X-ray loudness parameters (defined as $\mathcal{R}_X \equiv \nu L_{5\text{GHz,rf}}/L_{2-10\text{keV,rf}}$; see Sect. 4.2): $\sigma_{\mathcal{R}}/\mathcal{R}$ and $\sigma_{\mathcal{R}_X}/\mathcal{R}_X$, of 0.11 and 0.3 (radio-detected), and 0.10 and 0.19 (radio-undetected), respectively.

4. Radio loudness

The importance of the radio emission in a source is generally described using the radio-loudness parameter. In this paper, we adopt the definition with the reference band in the UV, a range less affected by the host galaxy contribution (Stocke et al. 1992):

$$\mathcal{R} \equiv \frac{F_{5\text{GHz,rf}}}{F_{2500\text{\AA,rf}}} \quad (3)$$

instead of the classical ratio with respect to optical *B*-band flux. As done previously, the UV continuum flux was calculated using the QSO template, normalized to the continuum flux under the Mg II line, as reported in the *SDSS* catalogue. About 29 QSOs are in common with Strateva et al. (2005), where the authors calculated luminosities by fitting *SDSS* spectra (after dereddening and correcting for fibre inefficiencies, and also subtracting host-galaxy emission). Comparing the UV luminosities for these sources, we find close agreement (mean difference of

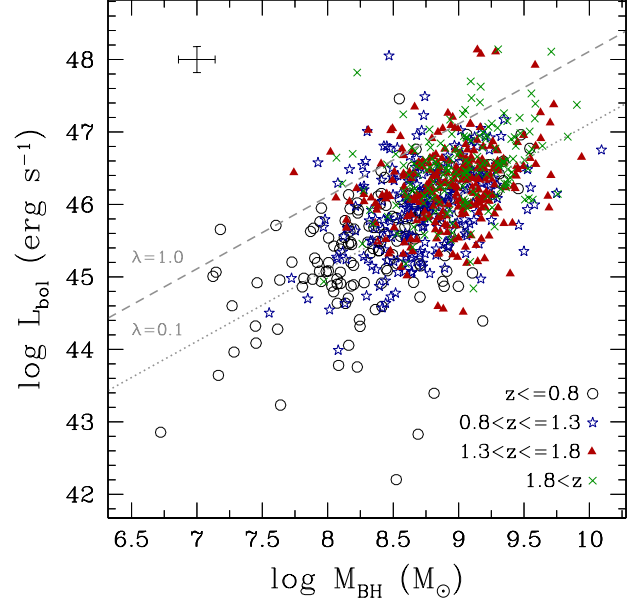


Fig. 4 Bolometric luminosities vs. black hole masses for the sample of X-ray emitting type 1 AGN, divided in intervals of redshift ($z \leq 0.8$, black open circles; $0.8 < z \leq 1.3$, blue open stars; $1.3 < z \leq 1.8$, red filled triangles; $z > 1.8$, green crosses). Only mean error bars are reported to avoid clutter. Grey dashed and dotted lines define the locus for sources emitting at the Eddington limit and at 1/10 of it.

$\Delta \log L_{2500\text{\AA}} < 3\%$, with a standard deviation of 0.1). This result reassures us on the accuracy of our approach.

For the 74 detected sources in the “main sample”, as well as for the “control sample”, the radio flux was obtained from the FIRST integrated flux density at 1.5 GHz (observed frame; FINT), assuming a power-law spectrum $F_\nu \propto \nu^{-\alpha}$ with index $\alpha = 0.5$. For the 737 nondetected sources, from the flux limit of the FIRST survey ($F_{1.5\text{GHz,obs}}^{\text{lim}} = 1\text{ mJy}$) and the optical flux, we calculated an upper limit to the radio-loudness parameter. The distributions of both \mathcal{R} and $\mathcal{R}^{\text{up.lim}}$ for the “main sample” are shown in Figure 5 (*left panel*). The radio properties of the subsample falling in the FIRST fields are reported in Table 5; the second part of the Table contains the same quantities for the 11 X-ray-undetected sources in the “control sample”.

From Figure 5 (*left panel*), it is evident that the detected sample is distributed rather uniformly in terms of the \mathcal{R} parameter (green shaded histogram). As thresholds, we assumed $\mathcal{R} = 10$ and $\mathcal{R} = 1$ (values typically used in literature, e.g. Miller et al. 2011). Out of the 74 detected sources, 59 are RL (all but two QSOs) and 15 have a radioloudness parameter intermediate between the two boundary values (RI, all QSOs); we have no detected RQ. The 7 nondetected sources with $\mathcal{R}^{\text{up.lim}} < 1$ can be safely classified as RQ, while for the 443 radio-undetected AGN with $1 < \mathcal{R}^{\text{up.lim}} \leq 10$ we can only exclude a RL classification. Finally, for the 287 undetected sources with $\mathcal{R}^{\text{up.lim}} > 10$, we are not able to give a radio-loudness classification.

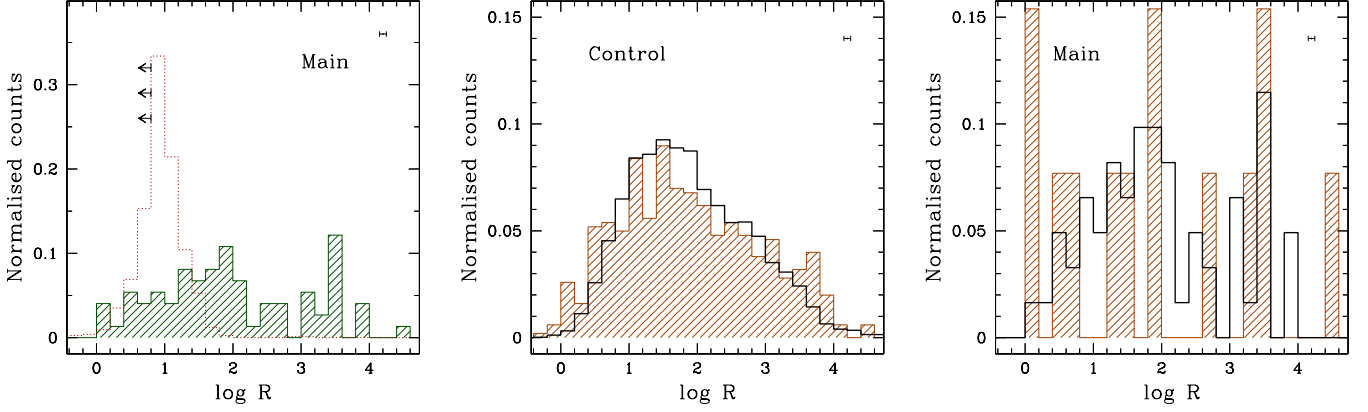


Fig. 5 Normalised distributions of radio-loudness parameter \mathcal{R} , derived as described in Sect. 3; the error bars reported represent the mean uncertainties obtained as detailed in Sect. 3.4. *Left panel*: radio-detected (green shaded histogram) and radio-undetected (red dotted line) sources in the “main sample”. *Central panel*: *ROSAT*-detected (brown shaded histogram) and *ROSAT*-undetected (black continuous line) sources in the “control sample”. *Right panel*: radio-detected sources in the “main sample”, divided between *ROSAT*-detected (brown shaded histogram) and *ROSAT*-undetected (black continuous line).

For the QSOs with sensitive radio measurements, P. Francis produced sub-composites of RL and RQ⁷. We checked the UV fluxes and our radio-loudness classification, both derived assuming the total composite QSO spectrum, using the two sub-composites; the results are in agreement within the errors.

The lack of a clear dichotomy in the distribution of \mathcal{R} is in agreement with the trend of recent works showing that the classical gap between RL and RQ fills up when deeper and complete samples are considered (e.g., Miller et al. 2011). A different result might be obtained if the narrow distribution of upper limits to \mathcal{R} (red dotted line in Fig. 5, *left panel*) corresponds to a broader real distribution, peaking at lower values. In particular, the radio-detected subsample is characterized by a rather high \mathcal{R} , median value ~ 1200 . This could be partially due to a selection bias: if high X-ray emission implies high enough radio emission, the X-ray selection can cause a loss of RQ sources.

The distribution of \mathcal{R} for radio sources for which upper limits to the X-ray emission are available would give important information to confirm or deny this hypothesis. Unfortunately, the low number of AGN with X-ray upper limits in the “control sample” (11/4508) prevents us from drawing firm conclusions, although their distribution seems consistent with that found for the “main sample”. This suggestion is reinforced when we consider the match with the RASS: comparing the \mathcal{R} distribution of *ROSAT*-detected (501 out of 4508) and *ROSAT*-undetected sources in the “control sample”, we found no statistical difference in terms of radio loudness (KS probability of 0.11; see Fig. 5, *central panel*). The same result is obtained when considering the radio-detected sources in the “main sample”: comparing *ROSAT*-detected (13 out of 67) and *ROSAT*-undetected sources, the hypothesis of the same original population is confirmed with a KS probability of 0.68 (see Fig. 5, *right panel*); this means that a detection or non-detection by *ROSAT* does not relate to radio-loudness. The same appears to be true (albeit with a much smaller sample) for *XMM-Newton* hard X-ray detection or non-detection.

⁷ See http://msowwww.anu.edu.au/pfrancis/composite/lbqs_rl_comp.d and http://msowwww.anu.edu.au/pfrancis/composite/nonbal_rq_comp.d, respectively

Table 2 Radio loudness properties in redshift bins.

		$z < 0.7$	$0.7 \leq z < 1.1$	$1.1 \leq z < 1.5$	$1.5 \leq z < 1.8$	$z \geq 1.8$
(1)	(2)	(3)	(4)	(5)	(6)	(7)
“main”	RL	9	13	18	8	11
	det. RI	8	2	4	0	1
	$\mathcal{R}^{up,lim} \in (1, 10]$	48	96	114	94	91
	RQ	3	0	2	1	1
“control”	RL	827	772	953	708	536
	det. RI	200	171	138	98	95
	RQ	3	4	0	1	2

(1) Sample. (2) Radio loudness classification. (3)-(7) Redshift bins.

The wide range in redshift spanned by our sample can introduce evolutionary effects in the observed distribution of \mathcal{R} parameters. To evaluate its importance, we divided our sample in 5 bins of redshift, having a comparable number of sources. We do not find clear evidence of redshift evolution in the RL population: the change in the χ^2 when a constant is replaced with a straight line (from 2.12 to 1.35) implies an F-test probability $P_F \sim 0.28$. On the other hand, the high number of upper limits compared with the number of detected RI does not allow us to draw firm conclusions regarding the evolutionary pattern in this subclass. Again, to better investigate the evolutionary effects, we would need detections instead of upper limits. From the present data, we conclude that the size and depth of our sample is the main reason of filling the gap between RL and RQ, rather than evolutionary effects. If they exist, they must developed well after the QSO peak epoch studied here.

4.1. Eddington ratios vs radio-loudness

Comparing Eddington ratios and radio-loudness for the sources falling in the FIRST survey area, we see an apparent trend of increasing \mathcal{R} with λ_{Edd} (see Fig. 6). We checked the significance of the correlation using both a generalized Kendall rank correlation test ($\tau_k > 0.1$) and a Spearman rank correlation test ($\rho_s > 0.15$), finding a probability \mathcal{P} lower than 0.1% in both cases that a correlation is present only due to chance. We used the

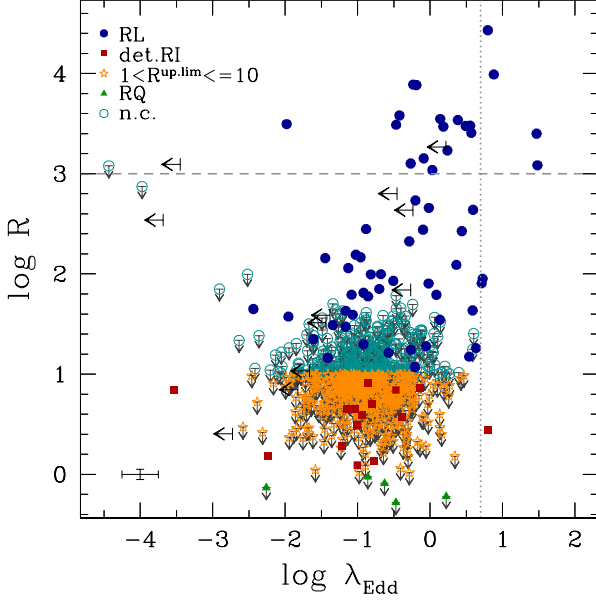


Fig. 6 Radio-loudness parameters vs. Eddington ratios. Key as in Fig. 3: RL, blue filled circles; detected RL, red filled squares; undetected sources with $\mathcal{R}^{\text{up.lim}} \in (1, 10]$, yellow open stars; RQ, green filled triangles; not classified, light-blue open circles. Undetected sources are also marked with small grey arrows. Only mean error bars are reported to avoid clutter. Big black arrows correspond to the upper limits found for the 11 X-ray non-detected sources in the “control sample”. The vertical dotted line marks the threshold of $\lambda_{\text{Edd}} = 5$, while the horizontal dashed line corresponds to $\mathcal{R} = 1000$.

ASURV package (Feigelson & Nelson 1985; Isobe et al. 1986, Astronomy Survival Analysis), that facilitates a correct statistical analysis when censored data (upper limits in this case) are present, although the errors are not considered in the calculations. This positive correlation is in contrast with previous results, that found an increase of radio loudness with decreasing Eddington ratio (e.g., Ho 2002; Merloni et al. 2003; Nagar et al. 2005; Sikora et al. 2007). We note, however, the different range covered, narrower both in \mathcal{R} and λ_{Edd} in our sample than in previous works (e.g., Sikora et al. 2007, $\log \mathcal{R}$ between -2 and 7 , and $\log \lambda_{\text{Edd}}$ between -6.6 and 0.7 ; cf. their fig. 3).

The higher Eddington ratios observed for sources more RL could either denote a difference in the accretion mechanisms powering AGN with different radio-loudness, or can be related to our assumptions when calculating L_{bol} . Note that using a constant X-ray bolometric correction, $\kappa_{2-10 \text{ keV}} = 50$, instead of a luminosity-dependent one, the distribution of λ_{Edd} would become a little narrower but without changing in any significant way our results.

In principle, in RL sources the observed X-ray flux could be “contaminated” by contribution from a kpc-, or even pc-scale X-ray jet emission, not resolvable with XMM-Newton, making problematic to recover the accreting bolometric luminosities. The fraction of X-ray emission in RL AGN that is from the jet, is a strongly debated issue. The spurious non-nuclear emission is typically observed to be only a few percent as bright as the X-ray core (e.g., Marshall et al. 2005), which would not significantly change the calculated $L_{2-10 \text{ keV}}$ values. Figure 3 confirms these

considerations, suggesting that the overestimate of L_{bol} due to jet contamination is relatively low.

Otherwise, the spectral energy distribution (SED) may be different in RL and RQ AGN, with a coronal contribution much more important with respect to the optical emission in the former than in the latter. In this case, applying a $\kappa_{2-10 \text{ keV}}$ bolometric correction obtained mainly from RQ AGN would overestimate the optical emission, leading to a bolometric luminosity too high. Indeed, because of these difficulties in determining the true SED linked to the accretion disk, most studies of the X-ray bolometric correction have been performed excluding RL sources from the study of the nuclear properties. In the sample studied by Vasudevan & Fabian (2007), RL objects occupy the region of higher hard X-ray luminosities and lower X-ray bolometric correction (see their fig. 3). For one object, 3C 273, the authors are able to estimate the importance of the jet contribution, comparing old ASCA data with new XMM-Newton observations taken at a historic jet minimum. Interestingly, despite an increasing of $\kappa_{2-10 \text{ keV}}$ that moves the object in the upper-left direction in the $\kappa_{2-10 \text{ keV}}$ vs. $L_{2-10 \text{ keV}}$ diagram, 3C 273 still falls significantly below the Marconi et al. (2004) relation.

In most cases, the quality of the X-ray data does not allow us to perform a detailed spectral analysis. We limited ourselves to check whether the hardness ratios (HR s) of the two classes are compatible with a steeper, accretion-dominated spectrum or with a flatter spectrum; the latter could be due to a jet-dominated emission, or to a different disk-corona structure. This analysis allows us to investigate, at least from a statistical point of view, also the presence of intrinsic absorption, trying to quantify its effects.

We considered HR s defined from both soft and hard bands, dividing the “main sample” into RL (59) and non-RL (465; see Table 1); the 287 non-classified sources are excluded from the HR analysis. The hard hardness ratio, $HR_{\text{hard}} \equiv C[2 - 4.5]/C[4.5 - 12]$ (where $C[2 - 4.5]$ and $C[4.5 - 12]$ are the vignetting-corrected count-rates between 2 and 4.5 keV observed frame, and between 4.5 and 12 keV observed frame, respectively), less affected by absorption, is more directly linked with nuclear emission than the HR constructed from the whole X-ray band. On the other hand, comparing $HR_{\text{tot}} \equiv C[0.2 - 2]/C[2 - 12]$ (where $C[0.2 - 2]$ and $C[2 - 12]$ are the vignetting-corrected count-rates between 0.2 and 2 keV observed frame, and between 2 and 12 keV observed frame, respectively) can provide information on the possible presence of absorption. Indeed, the spectral modification induced in a typical AGN spectrum by matter absorbing the nuclear emission, can mimic, in the total hardness ratio, a flatter (or even inverted) power law.

In Figure 7 we show the observed distributions for RL (*upper panels*) and non-RL (*bottom panels*) sources (hard HR_{hard} , *left panels*; total HR_{tot} , *right panels*). From a KS test, the probability of the RL and non-RL subsamples being drawn from the same population is lower than 0.5% in terms of both HR s. We then compared the observed HR s with that expected from a jet-dominated or a disk-dominated emission (power law with $\Gamma = 1.4$ or $\Gamma = 1.9$, respectively), to investigate whether the X-ray colours reflect some difference in the components contributing to the observed emission. The distributions expected for the “main sample” assuming a simple power-law emission covered by Galactic absorption are overplotted to the observed ones in Figure 7. Note the slight broadening of the expected distributions of HR_{tot} , due to the absorption of our Galaxy and to the different redshifts of the sources.

The dispersion in the distributions is too large to allow us to draw firm conclusions. We note, however, that the HR_{hard}

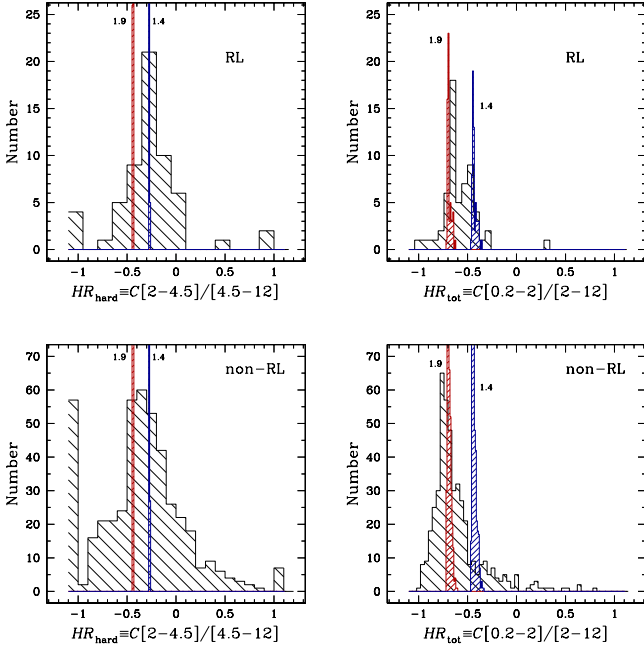


Fig. 7 Distributions of hard (*left panels*) and total (*right panels*) hardness ratios. Observed HR s: black shaded histograms. As a comparison, we show the HR s expected for jet-dominated ($\Gamma = 1.4$, blue shaded histogram), and disk-dominated emission ($\Gamma = 1.9$, red shaded histogram). The HR s distributions have been calculated for RL (*upper panels*) and non-RL sources (excluding the non-classified objects; *lower panels*).

suggest flatter photon indices for RL sources than for non-RL sources: $\langle HR_{\text{hard}}^{\text{RL}} \rangle = -0.27 \pm 0.37$ and $\langle HR_{\text{hard}}^{\text{non-RL}} \rangle = -0.34 \pm 0.42$, to be compared with $HR_{\text{hard}, 1.9} \sim -0.44$ and $HR_{\text{hard}, 1.4} \sim -0.27$. On the other hand, HR_{tot} is not consistent with a strong jet contribution for both RL and non-RL sources: $\langle HR_{\text{tot}}^{\text{RL}} \rangle = -0.58 \pm 0.18$ and $\langle HR_{\text{tot}}^{\text{non-RL}} \rangle = -0.62 \pm 0.27$, while $HR_{\text{tot}, 1.4} \sim -0.43$.

For $\sim 50\%$ of the non-RL subsample (238 sources), the analysis of the HR_{tot} suggests a photon index flatter than 1.9; we investigated the possible presence of absorption in this subsample. For each source, we calculated the expected HR_{tot} for an intrinsic power-law emission with $\Gamma = 1.9$, covered by a distribution of matter with N_{H} spanning from 10^{21} cm^{-2} to 10^{24} cm^{-2} . The observed ratios can be reconciled with the assumption of $\Gamma = 1.9$ assuming a column density lower than 10^{22} cm^{-2} for $\sim 63\%$ of the 238 sources. Interestingly, when the same exercise is performed for the whole subsample of RL + non-RL objects, all but two⁸ out of the 13 sources for which we found $N_{\text{H}} \geq 10^{23} \text{ cm}^{-2}$ are non-RL; as anticipated, however, the underestimate of the X-ray luminosity implied by our general assumption of unabsorbed power-law emission is lower than a factor of 3, not enough to affect the apparent trend observed in Figure 6.

Finally, we explored the nature of the most extreme sources, with higher \mathcal{R} and/or λ_{Edd} . Extremely beamed objects, in particular objects with featureless optical spectra, are mostly excluded from our sample by the optical selection criteria. However, in this range of radioloudness and/or accretion efficiency the contamination of Flat Spectrum Radio Quasars (FSRQs; blazars with the optical spectrum not totally swamped by the jet and

showing broad lines produced in the BLR) can be important, implying a strong contribution of the jet mainly in the X-ray band. Moreover, the overestimate of the X-ray emission would be amplified (due to the luminosity-dependent X-ray bolometric correction adopted) in calculating L_{bol} . From the literature, among the 7 sources with $\lambda_{\text{Edd}} > 5$, we found 3 blazars, 1 FR II, and 1 lensed QSO (lensing effects can make difficult to correctly estimate intrinsic luminosities); no information was found for the remaining 2 objects. The 11 out of 19 (all but 1 QSOs) radio-detected sources with $\mathcal{R} > 1000$, for which we found some information in the literature, are indeed classified as blazars or FR IIs. In the following discussion, we will exclude these 22 extreme sources, i.e. those with extreme $\mathcal{R} > 1000$ and/or $\lambda_{\text{Edd}} > 5$.

The exclusion of the extreme sources reduces the probability of a correlation between \mathcal{R} and λ_{Edd} (from a generalized Kendall rank correlation test: $\tau_k > 0.04$, $\mathcal{P}_k = 1.6\%$; from a Spearman rank correlation test: $\rho_s > 0.03$, $\mathcal{P}_s = 29\%$), suggesting an important effect of the most strongly jetted sources in drawing the apparent trend observed in Figure 6.

4.2. SED shape and luminosity-dependence

In the last years, several works have been published exploring the relation between the emission at different energies in AGN, as a possible indication of the mechanisms in action in samples spanning different ranges in their observational properties. In particular, many authors have investigated the relation between restframe UV and soft X-ray AGN emission, and its dependence with redshift and/or optical luminosity; note that RL sources are removed from the samples studied in most of these works. Most studies have concluded that there is no evidence for a redshift dependence, while the X-ray emission (i.e., the fraction of power in the accretion disk corona) is correlated with the UV emission, and the ratio of the monochromatic X-ray to UV luminosities, $\alpha_{\text{ox}} \equiv \log(F_{2 \text{ keV}}/F_{2500 \text{ \AA}})/\log(\nu_{2 \text{ keV}}/\nu_{2500 \text{ \AA}})$, decreases as the UV emission increases (Vignali et al. 2003; Strateva et al. 2005; Steffen et al. 2006; Just et al. 2007; Gibson et al. 2008). Our sources nicely fall along the mentioned correlations, as shown in Figure 8, with a scatter consistent with the spread in their best fits. Nevertheless, RL in general show an α_{ox} higher than expected, while detected RI lie around the regression line. Since the luminosity dependence in the Marconi et al. (2004) X-ray bolometric correction is implemented via the luminosity dependence of the α_{ox} spectral index, this result can affect our estimate of the L_{bol} values. However, the good agreement among the X-ray-based and the optical/UV-based estimates of L_{bol} (see Figure 3 and the discussion at the end of Sect. 3.2) suggests that the effect in our calculation is not significant.

The different weight of the X-ray emission with respect to the UV one, again, suggest a different spectral shape for sources with important radio emission. Although a contribution to the high-energy luminosity due to the jet (at least, higher than to the optical one), cannot be completely ruled out, the exclusion of the most extreme, jetted sources from the comparison shown in Figure 8 weakens this hypothesis. Note that the UV continuum is often found to be redder in RL than in RQ (e.g., Ivezić et al. 2002; Labita et al. 2008). In such a scenario, a larger α_{ox} in RL objects can be obtained by assuming a reduced UV continuum emission.

Looking at Figure 8, it is quite evident that 5 out of the 11 X-ray non-detected sources in the “control sample” (large upper limits in the upper and central panels) have $L_{2500 \text{ \AA}}$ significantly lower than the luminosity observed for the sources in the “main sample”. Since a significant difference between both samples in

⁸ An AGN not covered by FIRST and a source for which the FIRST UL does not allow to obtain a radio classification.

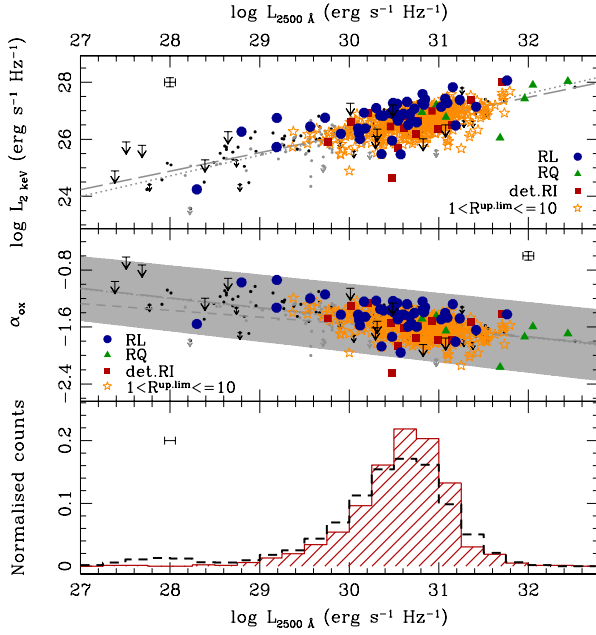


Fig. 8 Dependence on the 2500 Å monochromatic luminosity of $L_{2\text{keV}}$ (upper panel) and α_{ox} (central panel). Key as in Fig. 3: RL, blue filled circles; detected RI, red filled squares; undetected sources with $\mathcal{R}^{\text{up.lim}} \in (1, 10]$, yellow open stars; RQ, green filled triangles. Big arrows correspond to the upper limits found for the 11 X-ray non-detected sources in the “control sample”. Only mean error bars are reported to avoid clutter. Our data are compared with results found in the literature for samples of sources of different luminosities from the *SDSS*. Long-dashed lines are the best-fit linear relations for the samples by Strateva et al. (2005), updating the work of Vignali et al. (2003, dashed lines); the dotted line represents the best fit to the Steffen et al. (2006) sample. The grey-shaded area gives the spread in the Steffen et al. (2006) best fit. Black and grey filled circles mark the *SDSS* objects with $0.1 \leq z \leq 4.5$ from Strateva et al. (2005) and the data from Steffen et al. (2006, extending their work to a larger range in luminosities), respectively; arrows indicate upper limits in the X-ray detection. Lower panel: normalized distribution in $L_{2500\text{Å}}$ (red shaded histogram); the black dashed line shows the distribution for the “control sample”.

the UV luminosity would affect our analysis, we checked that these low luminosities are not representative of the values for the whole “control sample”. A comparison between the distributions in $L_{2500\text{Å}}$ of the two samples (see Figure 8, lower panel) demonstrates that the two samples cover similar ranges in UV luminosity, both peaking at $\sim 3 \times 10^{31} \text{ ergs s}^{-1} \text{ Hz}^{-1}$, with the distribution of the “control sample” extending down to lower luminosities, where about half of the X-ray non-detected sources can be found.

Comparing the radio-loudness with respect to different energy ranges (e.g., optical, UV, X-ray) can provide hints on the relations between the emission in the different bands, and/or their evolution with redshift or luminosity. In the following, we con-

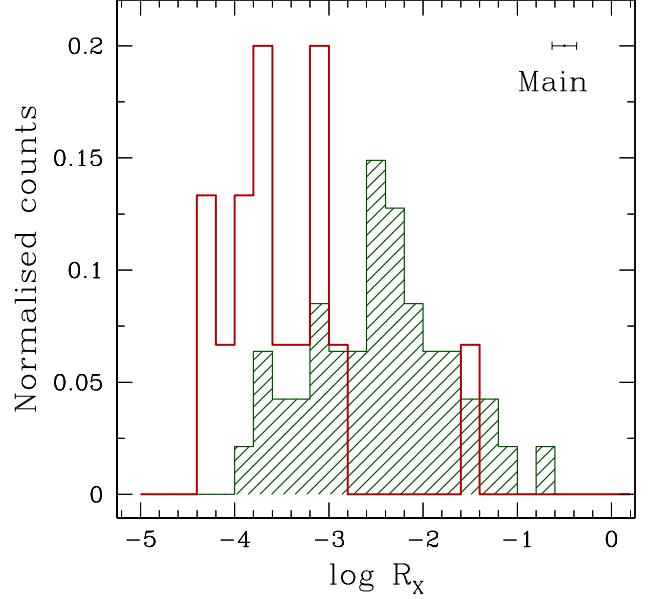


Fig. 9 Normalised distribution of \mathcal{R}_X for the radio-detected sources in the “main sample”. RL, green shaded histogram; detected RI, red continuous line. The error bar reported represents the mean uncertainties in \mathcal{R}_X , obtained as detailed in Sect. 3.4.

sider the radio loudness parameter with respect to the hard X-ray luminosity (Terashima & Wilson 2003):

$$\mathcal{R}_X \equiv \frac{\nu L_{5\text{GHz,rf}}}{L_{2-10\text{keV,rf}}} \quad (4)$$

The values of \mathcal{R}_X (or their upper limits, for radio-undetected sources) are reported in Table 5; in the second part, we report the lower limits to radio-to-X-ray ratio for the AGN in the “control sample” for which we have X-ray upper limits.

The distribution of \mathcal{R}_X for detected sources suggests the possible presence of a gap at $\log \mathcal{R}_X \sim -3$. However, whether it is real or not depends again on the distribution of undetected sources. All the RL sources (i.e., sources with $\mathcal{R} > 10$) have $\log \mathcal{R}_X > -4$; the distinction between RL and RI tends to disappear, having 12 out of 15 detected RI \mathcal{R}_X higher than this threshold (see Fig. 9).

The dependence of these boundaries with the luminosity is still an open issue. For a sample of local Seyfert galaxies and low-luminosity radio galaxies, Panessa et al. (2007) found for RL/non-RL separating values of $\log \mathcal{R}_X \sim -2.8$ and $\log \mathcal{R}_{4400} \sim 2.4$, while the addition of luminous PG quasars implies a $\log \mathcal{R}_X \sim -4.5$, fixing $\mathcal{R}_{4400} = 10$ to define RL sources (Terashima & Wilson 2003).

Note that the radio-to-optical loudness was calculated by Terashima & Wilson (2003) and Panessa et al. (2007) using the optical luminosity at 4400 Å instead of the UV luminosity at 2500 Å. Therefore, to properly compare the our “main sample” and the low-luminosity sample by Panessa et al. (2007), we have to evaluate the same parameter, \mathcal{R}_{4400} . Again, to estimate the optical luminosity at such wavelength, we adopted the QSO template, normalized to the continuum flux under the nearest feature to this wavelength, in this case the $H\beta$ line, as reported in the *SDSS* catalogue. This means that a comparison can be performed

only for the 185 sources showing this line in their *SDSS* spectra. As before, for the radio nondetected sources we calculated an upper limit to the optical radio-loudness parameter from the flux limit of the FIRST survey. We note that our approach could possibly overestimate the 4400 Å flux by including host galaxy emission, that can contribute to the optical band, in a particularly significant way for AGN with lower optical luminosity. In these sources, the resulting \mathcal{R}_{4400} values come out smaller than the real one.

The results are reported in Table 5; the second part of the Table contains the same quantities for the 11 X-ray-undetected sources in the “control sample”. The $\log \mathcal{R}_{4400}$ versus $\log \mathcal{R}_X$ is shown in Figure 10 (*left panel*); in the same plot we report also the Panessa et al. (2007) sample. Clearly, our sample falls below both correlations found by Terashima & Wilson (2003) and Panessa et al. (2007); this is observed apart from the classification in terms of \mathcal{R} , although the effect is more evident for sources with lower \mathcal{R} .

The main result we can draw is that the increase in the emission in the X-ray and radio bands seems to proceed in a linked way: higher X-ray luminosity corresponds to higher radio luminosity, so that the range spanned in \mathcal{R}_X is roughly the same. On the contrary, the optical luminosity changes independently, producing the observed decrease in \mathcal{R}_{4400} . We note that the large fraction of radio upper limits in our sample can partially affect all the considerations we are doing: detections instead of upper limits could in principle change the overall distribution of our sample in the different distribution diagrams.

A possibility is that the former connection is just apparent, mainly due to a strong contamination of the X-ray observed emission due to the jet, i.e. the same physical component where the radio emission is produced. However, in the previous sections we excluded the presence of a significant contribution of X-rays from the jet. Moreover a direct comparison between the 2 – 10 keV luminosity and the radio luminosity at 6 cm demonstrates that this is not the case (see Fig. 10, *central panel*). As expected, we are sampling a range of higher luminosities both at short and long wavelengths. At lower and intermediate radio luminosities our sample falls along the best-fit line found by Panessa et al. (2007) for their Seyferts (dotted line). More interestingly, an effect of “saturation” seems to take place, with the sources at higher luminosities (mainly RL) shifting towards the locus of low-luminosity radio galaxies. This result reinforces our former conclusion that the X-ray luminosity is not jet-dominated, even in RL sources, confirming in addition our X-ray-based estimation of nuclear properties. Therefore, we are left with the only conclusion that we are looking at a real different relation between the jet and (on one side) the regions where X-rays are emitted and (on the other side) the regions where optical radiation is produced. While the presence of jet changes the structure of the BH-accretion disk-corona systems so that the X-ray emission is strongly affected, the effects on the observed optical emission is lower, since the contribution from the most external region of the disk basically is likely untouched. Quite interestingly, Cleary et al. (2007), investigating the MIR properties in a sample of extremely powerful radio sources with *Spitzer*, found an “upper envelope” in the observed 15 μm luminosity for the most powerful RL AGN. In their analysis the authors suggest that, if observed at higher radio lobe luminosities than those of their sample, this may provide support for the “receding torus” model (Lawrence 1991). Assuming a MIR-to-X-ray ratio of ~ 10 (from the global SEDs of Richards et al. 2006), our observed saturation limit matches approximately their limit of $L_{15\mu\text{m}} = 10^{24.5} \text{ W Hz}^{-1} \text{ sr}^{-1}$.

The accretion regime in action in our sample is clearly different from that characterizing the Panessa et al. (2007) sample of Seyfert galaxies. The ratio between X-ray and Eddington luminosities is higher (see Fig. 10, *right panel*), while the importance of the radio emission with respect to the X-ray emission is comparable (see Fig. 10, *left panel*): although our sample spans a small range in Eddington ratios, looking at the radio-detected AGN (i.e., the blue filled circles, RL, and the red filled squares, detected RI, in Fig. 10) it seems that we are drawing a parallel track in the \mathcal{R}_X - \mathcal{R}_{4400} plane, moving at higher accretion. Again, the true distribution of the undetected sources (upper limits in both quantities, clustered at $\mathcal{R}_X \sim 10^{-4} - 10^{-3}$ and $\mathcal{R}_{4400} \sim 1 - 10$) may affect our conclusions. This important difference is confirmed when considering the so-called “fundamental plane of black hole activity” (Merloni et al. 2003, see Fig. 10, *right panel*): the majority of our AGN fall at accretion ratios higher than the threshold of $L_{2-10\text{keV}}/L_{\text{Edd}} > 10^{-3}$, where the switch between radiatively inefficient (ADAF) and radiatively efficient accretion flow is expected to occur. At these accretion regimes, the relation between accretion flow and jet power changes, as demonstrated by the deviation of our sample from the fundamental-plane equation (dotted line).

To summarize, we extend the analysis of the correlation between emission in different bands to higher luminosities for a wider sample of efficiently-accreting objects. The observed trend with the luminosity of the radio, optical, and X-ray emission and their correlations lead us to suggest that the radio emission is strongly coupled with a non-jet-dominated X-ray radiation, produced in the innermost region of the SMBH-accretion disk system, instead of with the optical one, which originates in a superposition of emission from material at different distances from the nucleus.

5. Conclusions

In this paper, we explored the interplay between X-ray and radio emission in type 1 AGN, in order to investigate the origin of radio emission in the framework of the AGN Unification Model, and its relation with the different physical components of the central system as well as with the different accretion regimes in act. The availability of deep catalogues at different energies, from radio up to X-rays bands, with wide sky coverage, allow us to collect multiwavelength information for a large sample of ~ 800 type 1 AGN, spanning a redshift range from 0.3 to 2.3.

For all the sources, we obtained the masses of the central black hole from the optical spectra, using the well-known relation between mass, emission-line width, and continuum luminosity. X-ray data were used to compute the bolometric output of the sources; being produced in the innermost regions of the central engine, the high-energy emission is one of the best proxies to estimate the bolometric luminosity, less affected by effects of reprocessing and external contamination than radiation emitted at larger distances. We tested our X-ray-based estimate of nuclear properties against the possible absorption in the X-ray band, finding that its effects would be negligible. In the previous sections, we discussed extensively the importance of the only contaminant we expect at high energy, i.e. the emission from the jet in the most powerful radio sources.

Combining SMBH masses and bolometric luminosities, we recovered the Eddington ratios; the collection of radio information allow us to characterize the sample in terms of importance of the radio emission in the global energetic output. We note that one of the main characteristics of this work is the derivation of the different physical quantities from observations in differ-

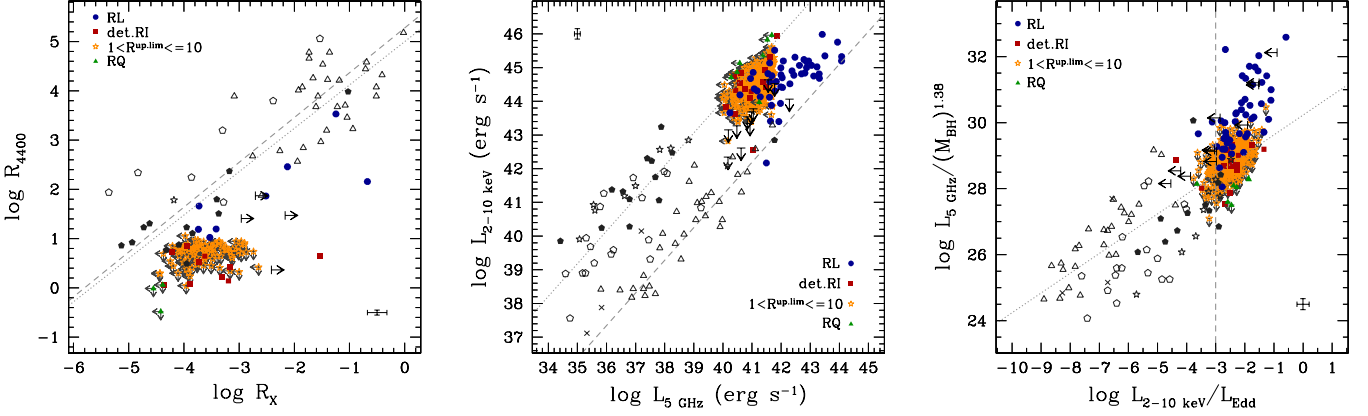


Fig. 10 *Left panel*: Relation between the radioloudness parameters \mathcal{R}_{4400} and \mathcal{R}_X ; dotted and dashed grey lines are the best-fit regression lines found by Terashima & Wilson (2003) and Panessa et al. (2007), respectively. *Central panel*: radio vs. X-ray luminosity; dotted and dashed grey lines are the best-fit regression lines found by Panessa et al. (2007) for Seyfert and low-luminosity radio galaxies, respectively. *Right panel*: X-ray-to-Eddington luminosity ratio compared to the AGN fundamental plan; dotted line corresponds to the fundamental plane equation, by Merloni et al. (2003), while vertical dashed line marks the L_X/L_{Edd} where the switch in the accretion mode is expected. Key as in Fig. 3: RL, blue filled circles; detected RI, red filled squares; undetected sources with $\mathcal{R}^{\text{up.lim}} \in (1, 10]$, yellow open stars; RQ, green filled triangles. Undetected sources are also marked with small grey arrows. Only mean error bars are reported to avoid clutter. Big black arrows correspond to the upper limits found for the 11 X-ray non-detected sources in the “control sample”. Our data are compared with the results found by Panessa et al. (2007) for a sample of low-luminosity AGN (grey symbols): filled and open polygons, Seyfert 1 and 2, respectively; open stars, Compton-thick candidates; crosses, “mixed Seyfert”; open triangles, low-luminosity radio galaxies.

ent energy ranges, compared with the unavoidable dependence expected when observations in the same energy band are used (e.g., the optical emission adopted both in the determination of the SMBH mass and as a proxy of the bolometric luminosity).

To assess whether these conclusions are a property related to the X-ray selection character of our sample, we tested our conclusions against a sample of FIRST radio AGN which appear in the *SDSS* catalogue, and for which X-ray information is obtained from the *ROSAT* All-Sky Survey (RASS; Voges et al. 1999).

Below we summarize our main results:

1. Our sources have typically $\lambda_{\text{Edd}} > 0.01$. The sample analysed, which is effectively X-ray selected, might be biased towards high accretion rates. It is not surprising then that the trend of \mathcal{R} increasing towards decreasing λ_{Edd} noted in local samples is absent in our study, as we do not expect ADAFs or other radio-prone low-efficiency accretion modes to be present. We also find a few extreme cases (both in terms of \mathcal{R} and λ_{Edd}), that we identify with beamed sources.
2. At a variance with lower-luminosity samples, ours does not show any hint of bimodality in radio-loudness. Despite the fact that our sample spans a wide redshift range, we have not found compelling evidence that bimodality develops with cosmic time. Although this cannot be excluded, we rather believe that the absence of a gap between RL and RQ is mainly due to the size of our sample, highly increased with respect to previous works. Our analysis suggests that, if the RL/RQ bimodality exist, it is a local effect.
3. We have computed X-ray loudness \mathcal{R}_X for RL and RQ AGN (excluding strongly jetted sources) and we conclude that in the bulk of the AGN population, radio emission is tightly linked to the accretion disk and not to larger scale phenomena.

Acknowledgements. Based on observations obtained with XMM-Newton (an ESA science mission with instruments and contributions directly funded by ESA

Member States and the USA, NASA). Funding for the *SDSS* and *SDSS-II* has been provided by the Alfred P. Sloan Foundation, the Participating Institutions, the National Science Foundation, the U.S. Department of Energy, the National Aeronautics and Space Administration, the Japanese Monbukagakusho, the Max Planck Society, and the Higher Education Funding Council for England. The *SDSS* Web Site is <http://www.sdss.org/>. The *SDSS* is managed by the Astrophysical Research Consortium for the Participating Institutions. This research has made use of NASA’s Astrophysics Data System. The research uses the interactive graphical viewer and editor for tabular data TOPCAT (<http://www.starlink.ac.uk/topcat/>) and its command-line counterpart STILTS (<http://www.starlink.ac.uk/stilts/>). We warmly thank the referee for her/his suggestions that significantly improved the paper. LB acknowledges support from the Spanish Ministry of Science and Innovation through a “Juan de la Cierva” fellowship. Financial support for this work was provided by the Spanish Ministry of Economy and Competitiveness through research grant AYA2010-21490-C02-01 FJHH acknowledges support from CSIC through the undergraduate research programme “JAE-Introducción a la investigación”.

References

- Abazajian, K. N., Adelman-McCarthy, J. K., Agüeros, M. A., et al. 2009, *ApJS*, 182, 543
 Becker, R. H., White, R. L., & Helfand, D. J. 1995, *ApJ*, 450, 559
 Begelman, M. C. 2002, *ApJ*, 568, L97
 Berti, E. & Volonteri, M. 2008, *ApJ*, 684, 822
 Blandford, R. D. 1990, in *Active Galactic Nuclei*, ed. R. D. Blandford, H. Netzer, L. Woltjer, T. J.-L. Courvoisier, & M. Mayor, 161–275
 Brinkmann, W., Laurent-Muehleisen, S. A., Voges, W., et al. 2000, *A&A*, 356, 445
 Cleary, K., Lawrence, C. R., Marshall, J. A., Hao, L., & Meier, D. 2007, *ApJ*, 660, 117
 Collin, S., Boisson, C., Mouchet, M., et al. 2002, *A&A*, 388, 771
 Collin, S. & Kawaguchi, T. 2004, *A&A*, 426, 797
 Eddington, A. S. 1913, *MNRAS*, 73, 359
 Elvis, M., Wilkes, B. J., McDowell, J. C., et al. 1994, *ApJS*, 95, 1
 Feigelson, E. D. & Nelson, P. I. 1985, *ApJ*, 293, 192
 Francis, P. J., Hewett, P. C., Foltz, C. B., et al. 1991, *ApJ*, 373, 465
 Garofalo, D., Evans, D. A., & Sambruna, R. M. 2010, *MNRAS*, 406, 975
 Gibson, R. R., Brandt, W. N., & Schneider, D. P. 2008, *ApJ*, 685, 773
 Ho, L. C. 2002, *ApJ*, 564, 120
 Hopkins, P. F., Richards, G. T., & Hernquist, L. 2007, *ApJ*, 654, 731

- Isobe, T., Feigelson, E. D., & Nelson, P. I. 1986, *ApJ*, 306, 490
- Ivezić, Ž., Menou, K., Knapp, G. R., et al. 2002, *AJ*, 124, 2364
- Jiang, L., Fan, X., Ivezić, Ž., et al. 2007, *ApJ*, 656, 680
- Just, D. W., Brandt, W. N., Shemmer, O., et al. 2007, *ApJ*, 665, 1004
- Kalberla, P. M. W., Burton, W. B., Hartmann, D., et al. 2005, *A&A*, 440, 775
- Kaspi, S., Maoz, D., Netzer, H., et al. 2005, *ApJ*, 629, 61
- Kaspi, S., Smith, P. S., Netzer, H., et al. 2000, *ApJ*, 533, 631
- Kellermann, K. I., Sramek, R., Schmidt, M., Shaffer, D. B., & Green, R. 1989, *AJ*, 98, 1195
- Labita, M., Treves, A., & Falomo, R. 2008, *MNRAS*, 383, 1513
- Lawrence, A. 1991, *MNRAS*, 252, 586
- Marchese, E., Della Ceca, R., Caccianiga, A., et al. 2012, *A&A*, 539, A48
- Marconi, A., Risaliti, G., Gilli, R., et al. 2004, *MNRAS*, 351, 169
- Marshall, H. L., Schwartz, D. A., Lovell, J. E. J., et al. 2005, *ApJS*, 156, 13
- Merloni, A., Heinz, S., & di Matteo, T. 2003, *MNRAS*, 345, 1057
- Miller, B. P., Brandt, W. N., Schneider, D. P., et al. 2011, *ApJ*, 726, 20
- Nagar, N. M., Falcke, H., & Wilson, A. S. 2005, *A&A*, 435, 521
- Osterbrock, D. E. 1989, *Astrophysics of gaseous nebulae and active galactic nuclei*, ed. Osterbrock, D. E.
- Panessa, F., Barcons, X., Bassani, L., et al. 2007, *A&A*, 467, 519
- Panessa, F., Bassani, L., Cappi, M., et al. 2006, *A&A*, 455, 173
- Pineau, F., Motch, C., Carrera, F., et al. 2011, *A&A*, 527, A126+
- Rees, M. J. 1984, *ARA&A*, 22, 471
- Richards, G. T., Lacy, M., Storrie-Lombardi, L. J., et al. 2006, *ApJS*, 166, 470
- Schneider, D. P., Richards, G. T., Hall, P. B., et al. 2010, *AJ*, 139, 2360
- Shen, Y., Richards, G. T., Strauss, M. A., et al. 2011, *ApJS*, 194, 45
- Sikora, M., Stawarz, Ł., & Lasota, J. 2007, *ApJ*, 658, 815
- Spergel, D. N., Bean, R., Doré, O., et al. 2007, *ApJS*, 170, 377
- Spergel, D. N., Verde, L., Peiris, H. V., et al. 2003, *ApJS*, 148, 175
- Steffen, A. T., Strateva, I., Brandt, W. N., et al. 2006, *AJ*, 131, 2826
- Stocke, J. T., Morris, S. L., Weymann, R. J., & Foltz, C. B. 1992, *ApJ*, 396, 487
- Strateva, I. V., Brandt, W. N., Schneider, D. P., Vanden Berk, D. G., & Vignali, C. 2005, *AJ*, 130, 387
- Terashima, Y. & Wilson, A. S. 2003, *ApJ*, 583, 145
- Vasudevan, R. V. & Fabian, A. C. 2007, *MNRAS*, 381, 1235
- Vestergaard, M., Fan, X., Tremonti, C. A., Osmer, P. S., & Richards, G. T. 2008, *ApJ*, 674, L1
- Vestergaard, M. & Osmer, P. S. 2009, *ApJ*, 699, 800
- Vestergaard, M. & Peterson, B. M. 2006, *ApJ*, 641, 689
- Vignali, C., Brandt, W. N., Schneider, D. P., et al. 2003, *AJ*, 125, 2876
- Voges, W., Aschenbach, B., Boller, T., et al. 1999, *A&A*, 349, 389
- Watson, M. G., Schröder, A. C., Fyfe, D., et al. 2009, *A&A*, 493, 339
- White, R. L., Becker, R. H., Gregg, M. D., et al. 2000, *ApJS*, 126, 133
- Wilson, A. S. & Colbert, E. J. M. 1995, *ApJ*, 438, 62

Table 3. Basic information for the 852 X-ray selected +11 X-ray undetected *SDSS* type 1 AGN.

2XMMi					SDSS								
SRCID (1)	R.A. (2)	Dec. (3)	$F_{0.2-12\text{ keV}}$ (4)	Redshift (5)	specObjID (6)	R.A. (7)	Dec. (8)	g_{SDSS} (9)	r_{SDSS} (10)	i_{SDSS} (11)	$\sigma(\text{Mg II})$ (12)	$F_c@2799\text{ \AA rf}$ (13)	FINT@1.5 GHz obs (14)
<i>X-ray detected AGN</i>													
192021	2.5419	0.8575	20.625 ± 3.563	0.3871 ± 0.0011	109716225189216256	2.5418	0.8574	19.210	18.685	18.475	9.878 ± 2.875	5.367	<i>undet.</i>
192103	2.8767	0.9644	38.860 ± 2.617	1.4934 ± 0.0014	109434742759227392	2.8767	0.9644	20.411	20.308	20.136	37.148 ± 5.183	3.405	156.0718 ± 0.1049
192150	5.5413	0.2747	4.366 ± 1.169	0.5749 ± 0.0012	110279119400337408	5.5415	0.2748	18.043	18.066	17.918	13.672 ± 0.477	21.257	<i>OutFIRST</i>
192335	7.5410	-0.3762	9.835 ± 13.374	0.4099 ± 0.0011	110560641432944640	7.5411	-0.3760	19.334	19.102	18.828	19.375 ± 1.788	6.224	<i>undet.</i>
[...]													
<i>X-ray undetected AGN</i>													
01Xund	126.6892	26.5414	< 0.833	0.3783 ± 0.0002	446646711809474560	126.6892	26.5414	20.266	19.026	18.388	84.222 ± 49.750	0.142	1.3000 ± 0.1310
02Xund	130.1848	19.6289	< 1.069	0.4500 ± 0.0002	641149183918604288	130.1848	19.6289	21.879	20.220	19.486	99.959 ± 48.131	0.908	2.5000 ± 0.1350
03Xund	131.8893	34.9104	< 1.188	1.0282 ± 0.0020	263123853125877760	131.8893	34.9104	19.447	19.148	19.139	23.386 ± 1.242	6.918	0.6400 ± 0.1510
04Xund	149.6652	30.8494	< 17.833	0.9730 ± 0.0013	549105712635052032	149.6652	30.8494	20.258	19.767	19.559	31.507 ± 2.546	4.270	3.7400 ± 0.1430
[...]													

Notes. The complete table is published in its entirety in the electronic edition of the journal. A portion is shown here for guidance regarding its form and content. In the first part, we list the X-ray detected AGN; in the second part, we report basic data for the 11 sources in the “control sample” undetected in the X-ray (see text).

Col. (1) : Unique source identification number in the 2XMMi catalogue; for the X-ray undetected sources, arbitrary ID number. Col. (2) & (3): J2000 right ascension and declination of the X-ray object (in degree). Col. (4): XMM-Newton EPIC-pn flux between 0.2 and 12 keV (entry `xmm_pn_8_flux` in the 2XMMi catalogue), in units of 10^{-14} ergs cm $^{-2}$ s $^{-1}$; for the X-ray undetected sources, XMM-Newton EPIC upper limit to the flux from FLIX. Col. (5): Redshift for the *SDSS* counterpart. Col. (6): Unique spectroscopic ID in the *SDSS* catalogue. Col. (7) & (8): J2000 right ascension and declination of the optical object (in degree). Col. (9) - (11): Magnitudes in the *g*, *r*, and *i* *SDSS* filters. Col. (12): Standard deviation of the Gaussian fitted to the Mg II line (in Å). Col. (13): Continuum value below the Mg II line (in units of 10^{-17} ergs cm $^{-2}$ s $^{-1}$ Å $^{-1}$). Col. (14): Integrated radio flux density at 1.5 GHz (observed frame; in units of mJy), from the FIRST survey; *OutFIRST*: source not covered by FIRST; *undet.*: source covered but not detected by FIRST.

Table 4. Derived properties for the 852 X-ray selected +11 X-ray undetected *SDSS* type 1 AGN.

SRCID (1)	Redshift (2)	$N_{\text{H,gal}}$ (3)	FWHM(Mg II) (4)	$\log L_{\text{cont}}@3000 \text{ \AA} \text{ rf}$ (5)	$\log M_{\text{BH}}$ (6)	$\log L_{2-10 \text{ keV}}$ (7)	$\log (L_{2-10 \text{ keV}}/L_{\text{Edd}})$ (8)	$\log \kappa_{2-10 \text{ keV}}$ (9)	$\log L_{\text{bol}}$ (10)	$\log \lambda_{\text{Edd}}$ (11)
<i>X-ray detected AGN</i>										
192021	0.3871 ± 0.0011	2.77	1294.88 ± 519.92	40.600 ± 0.049	7.123 ± 0.350	43.722 ± 0.075	-1.515 ± 0.358	1.287 ± 0.029	45.009 ± 0.080	-0.228 ± 0.359
192103	1.4934 ± 0.0014	2.66	3392.79 ± 1235.12	42.009 ± 0.008	8.664 ± 0.316	45.411 ± 0.029	-1.367 ± 0.318	1.936 ± 0.011	47.348 ± 0.031	0.569 ± 0.318
192150	0.5749 ± 0.0012	2.75	2163.19 ± 125.94	41.610 ± 0.004	8.074 ± 0.051	43.455 ± 0.116	-2.732 ± 0.127	1.184 ± 0.045	44.639 ± 0.125	-1.549 ± 0.135
192335	0.4099 ± 0.0011	2.42	3964.57 ± 544.14	40.683 ± 0.020	8.136 ± 0.120	43.454 ± 0.591	-2.797 ± 0.603	1.183 ± 0.227	44.637 ± 0.633	-1.614 ± 0.644
[...]										
204283	0.9268 ± 0.0029	3.15	$2056.91 \pm 608.64^{(*)}$	$41.245 \pm 0.008^{(*)}$	$7.848 \pm 0.607^{(*)}$	43.500 ± 0.420	-2.462 ± 0.738	1.201 ± 0.162	44.700 ± 0.451	-1.261 ± 0.756
[...]										
<i>X-ray undetected AGN</i>										
01Xund	0.3783 ± 0.0002	3.46	$15411.71 \pm 12547.71^{(*)}$	$38.915 \pm 0.008^{(*)}$	$8.432 \pm 0.896^{(*)}$	< 42.343	< -4.202	< 0.756	< 43.099	< -3.447
02Xund	0.4500 ± 0.0002	2.38	$17386.85 \pm 12139.42^{(*)}$	$39.920 \pm 0.008^{(*)}$	$9.039 \pm 0.819^{(*)}$	< 42.612	< -4.541	< 0.859	< 43.471	< -3.682
03Xund	1.0282 ± 0.0020	2.93	2923.67 ± 254.74	41.857 ± 0.005	8.459 ± 0.076	< 43.533	< -3.040	< 1.214	< 44.747	< -1.826
04Xund	0.9730 ± 0.0013	1.89	3359.55 ± 766.75	41.547 ± 0.011	8.425 ± 0.198	< 44.634	< -1.905	< 1.637	< 46.271	< -0.268
[...]										

Notes. The complete table is published in its entirety in the electronic edition of the journal. A portion is shown here for guidance regarding its form and content. In the first part, we list the X-ray detected AGN; in the second part, we report basic data for the 11 sources in the parent sample undetected in the X-ray (see text).

Col. (1): Unique source identification number in the 2XMMi catalogue; for the X-ray undetected sources, arbitrary ID number (as in Table 3). Col. (2): Redshift for the *SDSS* counterpart (as in Table 3). Col. (3): Galactic column density, from Kalberla et al. (2005); in units of 10^{20} cm^{-2} . Col. (4): FWHM of the Mg II emission line, in units of km s^{-1} ; for sources marked with (*), from the *SDSS* DR7 catalogue, otherwise from Shen et al. (2011). Col. (5): Monochromatic continuum luminosity at 3000 \AA rest frame, in units of $\text{ergs s}^{-1} \text{ \AA}^{-1}$; for sources marked with (*) recovered as described in Sect. 3, otherwise from Shen et al. (2011). Col. (6): Mass of the central BH, in units of M_{\odot} ; for sources marked with (*), computed from eq. (1); otherwise from Shen et al. (2011). Col. (7): Hard X-ray luminosity, recovered as described in Sect. 3; in units of ergs s^{-1} (upper limit for sources undetected in the X-ray). Col. (8): Ratio between the hard X-ray luminosity and the Eddington luminosity, $L_{\text{Edd}} \equiv 1.3 \times 10^{38} M_{\text{BH}}/M_{\odot} [\text{ergs s}^{-1}]$ (upper limit for sources undetected in the X-ray). Col. (9): Luminosity-dependent X-ray bolometric correction, from equation (2), (Marconi et al. 2004); upper limit for sources undetected in the X-ray. Col. (10): Bolometric luminosity, recovered as described in Sect. 3; in units of ergs s^{-1} (upper limit for sources undetected in the X-ray). Col. (11): Eddington ratio, defined as $\lambda \equiv L_{\text{bol}}/L_{\text{Edd}}$ (upper limit for sources undetected in the X-ray).

Table 5. Radio properties for the 852 X-ray selected +11 X-ray undetected *SDSS* type 1 AGN.

SRCID (1)	$F_{\text{rf}}@2500 \text{ \AA}$ (2)	α_{ox} (3)	$F_{\text{rf}}@4400 \text{ \AA}$ (4)	$F_{\text{rf}}@5 \text{ GHz}$ (5)	$F_{\text{rf}}^{\text{lim}}@5 \text{ GHz}$ (6)	\mathcal{R} (7)	$\mathcal{R}^{\text{up.lim}}$ (8)	Class. (9)	$\mathcal{R}_{4400 \text{ \AA}}$ (10)	$\mathcal{R}_{4400 \text{ \AA}}^{\text{up.lim}}$ (11)	\mathcal{R}_{X} (12)	$\mathcal{R}_{\text{X}}^{\text{lim}}$ (13)
<i>X-ray detected AGN</i>												
192021	0.0258 ± 0.0007	-1.2251 ± 0.0292	0.0732 ± 0.0018	<i>undet.</i>	0.6451 ± 0.1754	<i>undet.</i>	24.983 ± 6.828	NC	<i>undet.</i>	8.812 ± 2.405	<i>undet.</i>	0.0002 ± 0.0001
192103	0.0529 ± 0.0015	-1.1479 ± 0.0122	–	134.9836 ± 7.8384	–	2550.286 ± 164.680	–	RL	–	–	0.0148 ± 0.0013	–
192150	0.1318 ± 0.0037	-1.7358 ± 0.044	0.1459 ± 0.0037	<i>OutFIRST</i>	<i>OutFIRST</i>	<i>OutFIRST</i>	<i>OutFIRST</i>	–	<i>OutFIRST</i>	<i>OutFIRST</i>	<i>OutFIRST</i>	<i>OutFIRST</i>
192335	0.0309 ± 0.0009	-1.3782 ± 0.2267	0.0616 ± 0.0015	<i>undet.</i>	0.6504 ± 0.1721	<i>undet.</i>	21.022 ± 5.594	NC	<i>undet.</i>	10.556 ± 2.806	<i>undet.</i>	0.0007 ± 0.0005
[...]												
<i>X-ray undetected AGN</i>												
01Xund	0.0007 ± 0.0001	< -0.9594	0.0281 ± 0.0007	0.8359 ± 0.1700	–	1236.742 ± 253.902	–	RL	29.700 ± 6.085	–	–	> 0.0068
02Xund	0.0048 ± 0.0001	< -1.1943	–	1.6489 ± 0.2886	–	345.411 ± 61.235	–	RL	–	–	–	> 0.0104
03Xund	0.0712 ± 0.0020	< -1.6124	–	0.4992 ± 0.1278	–	7.015 ± 1.807	–	dRI	–	–	–	> 0.0020
04Xund	0.0416 ± 0.0012	< -1.0559	–	2.8774 ± 0.3212	–	69.226 ± 7.971	–	RL	–	–	–	> 0.0008
[...]												

Notes. The complete table is published in its entirety in the electronic edition of the journal. A portion is shown here for guidance regarding its form and content. In the first part, we list the X-ray detected AGN; in the second part, we report basic data for the 11 sources in the parent sample undetected in the X-ray (see text).

Col. (1): Unique source identification number in the 2XMMi catalogue; for the X-ray undetected sources, arbitrary ID number (as in Table 3). Col. (2): Monochromatic optical continuum flux at 2500 \AA , recovered as described in Sectt. 3 and 4 (in units of mJy). Col. (3): X-ray-to-optical spectral index, $\alpha_{\text{ox}} \equiv \log(F_{2\text{keV}}/F_{2500 \text{ \AA}})/\log(\nu_{2\text{keV}}/\nu_{2500 \text{ \AA}})$; upper limit for sources undetected in the X-ray. Col. (4): Monochromatic optical continuum flux at 4400 \AA , recovered as described in Sectt. 3 and 4.2 (in units of mJy); “–”: source without $\text{H}\beta$ line in their spectra. Col. (5): Monochromatic radio flux at 5 GHz (rest frame; in units of mJy), recovered from the integrated flux density at 1.5 GHz assuming a power-law spectrum $F_{\nu} \propto \nu^{-\alpha}$ with index $\alpha = 0.5$, as described in Sect. 4; *OutFIRST*: source not covered by FIRST; *undet.*: source not detected by FIRST. Col. (6): For sources covered but not detected by FIRST, monochromatic radio flux limit at 5 GHz (rest frame; in units of mJy), calculated from the flux limit at 1.5 GHz of the FIRST survey, $F_{1.5 \text{ GHz}} = 1 \text{ mJy}$, assuming the same spectral shape ($F_{\nu} \propto \nu^{-\alpha}$ with index $\alpha = 0.5$). Col. (7): Radio-UV radioloudness parameter, defined as the ratio between the radio flux at 5 GHz and the optical flux at 2500 \AA , both rest frame; *OutFIRST*: source not covered by FIRST; *undet.*: source not detected by FIRST. Col. (8): For sources covered but not detected by FIRST, limit to the radio-UV radioloudness parameter, calculated from the limit to the radio flux at 5 GHz and the optical flux at 2500 \AA , both rest frame. Col. (9): Radio classification: RL = radioloud; dRI = detected radiointermediate; ndRI = nondetected with $1 < \mathcal{R}^{\text{up.lim}} \leq 10$; RQ = radioquiet; NC = nonclassified; “–” = source not covered by FIRST. Col. (10): Radio-optical radioloudness parameter, defined as the ratio between the radio flux at 5 GHz and the optical flux at 4400 \AA , both rest frame; *OutFIRST*: source not covered by FIRST; *undet.*: source with $\text{H}\beta$ line in its spectrum but not detected by FIRST; “–”: source (detected or not detected by FIRST) without $\text{H}\beta$ line in its spectrum. Col. (11): For sources covered but not detected by FIRST, limit to the radio-optical radioloudness parameter, calculated from the limit to the radio flux at 5 GHz and the optical flux at 4400 \AA , both rest frame; “–”: source without $\text{H}\beta$ line in its spectrum. Col. (12): Radio-X-ray radioloudness parameter, defined as the ratio between the radio luminosity at 5 GHz and the X-ray luminosity in the $2 - 10 \text{ keV}$ energy range; *OutFIRST*: source not covered by FIRST; *undet.*: source not detected by FIRST. Col. (13): For sources covered but not detected by FIRST, limit to the radio-X-ray radioloudness parameter, calculated from the limit to the radio luminosity at 5 GHz and the X-ray luminosity in the $2 - 10 \text{ keV}$ energy range. Note that for the X-ray detected AGN not detected by FIRST (first part), it is an upper limit, while for sources in the second part, radio-detected and X-ray undetected, it is a lower limit.